Materials Advances

ROYAL SOCIETY OF CHEMISTRY

PAPER

View Article Online
View Journal | View Issue

Cite this: *Mater. Adv.*, 2023, 4, 5252

A novel magnetic HS^--adsorptive nanocomposite photocatalyst (rGO/$CoMn_2O_4$–$MgFe_2O_4$) for hydrogen fuel production using H_2S feed†

Majid Ghanimati,[a] Mohsen Lashgari,*[ab] Fabio Montagnaro,[c] Vassilios Binas,[d] Michalis Konsolakis[e] and Marco Balsamo[c]

Received 5th September 2023,
Accepted 18th September 2023

DOI: 10.1039/d3ma00668a

rsc.li/materials-advances

Synthesis of low-cost, eco-friendly, semiconducting solar-energy materials with excellent photocatalytic activity [high surface area, good reactant adsorption, photon harnessing in the visible region, and low charge recombination] for application in pollutant conversion to hydrogen is of great importance from environmental remediation as well as green energy and fuel production perspectives. In the present work, a magnetic heterojunction of $CoMn_2O_4$/$MgFe_2O_4$ and reduced graphene oxide (rGO) was synthesized through a combined Hummers'/hydrothermal method. The obtained nanocomposite (rGO/$CoMn_2O_4$–$MgFe_2O_4$) was employed for photocatalytic conversion of H_2S feed into hydrogen fuel. Adsorption studies in the feed solution proved a good capability for the photocatalyst to adsorb HS^- reactant from the reaction medium. This effect was ascribed to the presence of the $CoMn_2O_4$ component, serving as a strong bisulfide adsorbent. VSM (vibrating sample magnetometry) analysis revealed that the magnetic property of the photocatalyst was due to the $MgFe_2O_4$ component. Photocatalytic investigations showed that the addition of rGO to the $CoMn_2O_4$/$MgFe_2O_4$ nanocomposite not only improves its reactant adsorption capacity, but also increases the photocatalyst surface area, enhances photon absorption, and suppresses the charge (e/h) recombination, which eventually boosts the photocatalyst activity to produce more hydrogen fuel (~1.5 times).

1. Introduction

Pollutant elimination and conversion into hydrogen fuel using effective, affordable semiconducting energy materials is a green and economic strategy towards environmental remediation and sustainable supplying of the fuel/energy demand.[1–4] One of the most dangerous and toxic pollutants is H_2S gas, generated on a large scale during various natural and industrial processes.[5–7] Facing the H_2S issue, the existing routes to solve the problem are the use of adsorbents, thermal decomposition, electrochemical and photo-splitting, and burning in an oxygen atmosphere (Claus process) with the aim of H_2S elimination and production of hydrogen, sulfur, or other value-added materials.[8–11] Among these methods, the utilization of photons (sunlight) and semiconducting photocatalyst materials is an easy and economical way to convert this harmful pollutant into hydrogen fuel, and has attracted the attention of many researchers in recent years.[12–14] In this regard, magnetic adsorbing nanocomposite materials look ideal because, at the end of the photoconversion process, the photocatalyst particles can be easily collected and separated from the reaction medium by using an appropriate magnet.[15–18] Furthermore, considering the factors such as: (1) the use of earth-abundant elements and affordable eco-friendly chemicals, (2) the attempt to reach a large surface area, strong absorption of photons, low charge recombination, and appropriate energy levels, and (3) the ability of the photocatalyst to adsorb reactant species, are crucial in the design and synthesis of effective photocatalyst materials for large-scale applications.[19,20] To achieve these goals, the rational synthesis of composite photocatalysts with tailored physicochemical properties is an effective strategy.[13,21,22]

Regarding the semiconducting components of the nanocomposite photocatalyst synthesized in this work, it is worth mentioning that $CoMn_2O_4$ is a narrow-bandgap p-type

[a] Department of Chemistry, Institute for Advanced Studies in Basic Sciences (IASBS), Zanjan 45137-66731, Iran. E-mail: Lashgari@iasbs.ac.ir; Fax: +98 24 33153232; Tel: +98 24 33153205
[b] Center for Research in Climate Change and Global Warming: Hydrogen and Solar Division, Zanjan 45137-66731, Iran
[c] Department of Chemical Sciences, University of Naples Federico II, Complesso Universitario di Monte Sant'Angelo, 80126 Napoli, Italy
[d] Institute of Electronic Structure and Laser (IESL), FORTH, Vasilika Vouton, GR-70013, Heraklion, Greece
[e] School of Production Engineering and Management, Technical University of Crete, GR-73100, Chania, Greece

† Electronic supplementary information (ESI) available. See DOI: 10.1039/d3ma00668a

semiconductor, which has been widely used for the photocatalytic degradation of organic pollutants.[23,24] Moreover, due to the presence of Co and Mn, strong hydrogen sulfide adsorption is anticipated for this material.[13,25–27] The disadvantage of this semiconductor is its high charge recombination, which can be solved by making a composite with an n-type semiconductor.[28,29] In the present study, $MgFe_2O_4$ was used as a narrow-bandgap n-type magnetic semiconductor. The photocatalytic application of this material has also been reported in the literature for degradation of organic pollutants and water splitting as well.[30,31]

Since H_2S photoconversion is a heterogeneous process and the conversion does not occur until the reactant species adsorb on the photocatalyst surface, the surface area plays a crucial role in the photocatalytic activity.[21,32–34] To increase the photocatalyst surface area and improve its sorption capability [photon absorption/harnessing and reactant adsorption], reduced graphene oxide (rGO) was employed and the ternary magnetic rGO/$CoMn_2O_4$–$MgFe_2O_4$ nanocomposite was synthesized for the first time and applied as an efficient photocatalyst for the production of hydrogen fuel using H_2S feed.

2. Experimental section

2.1 Synthesis of GO, rGO, $MgFe_2O_4$, $CoMn_2O_4$ and their nanocomposites

Graphene oxide (GO) was synthesized through a Hummers' method with some modifications.[35–37] For this purpose, 2 g graphite powder (particle size: 0.4–1.2 μm, purity: 99.9%; US Research Nanomaterials, Inc.) and 4 g $NaNO_3$ (99%; Fluka) were added to 100 mL of concentrated H_2SO_4 (98%; Merck). The obtained mixture was placed in an ice water bath inside a laboratory hood and stirred for 30 min. Without removing the reaction vessel from the bath, 4 g $KMnO_4$ (99%; Fluka) was gradually (bit by bit) added to the reaction solution and stirred for 4 h. The acidic viscous mixture obtained from the previous step was slowly added to a solution containing 100 mL of deionized water (DW) and 10 mL of H_2O_2 (30%; Merck) and stirred for 15 min. Then the precipitate obtained from this step was filtered and washed with dilute HCl (0.1 M) and thereafter rewashed several times with DW. At the end, the precipitate was dried at 70 °C for 12 h.

To prepare reduced graphene oxide (rGO), a chemical reduction method was applied.[38–41] Accordingly, 100 μL of hydrazine (a reducing agent; H_6N_2O, 80%, Merck) was added to 100 mL DW containing 0.3 g GO (synthesized in the previous stage). The mixture was then refluxed with stirring for 8 h at 80 °C. Finally, the resulting precipitate was filtered and dried after washing several times with DW.

For the synthesis of $CoMn_2O_4$ and $MgFe_2O_4$ semiconductors, a hydrothermal method was used.[42–46] For $CoMn_2O_4$, 50 mL of an aqueous solution containing 5 mmol of Co^{2+} ($Co(NO_3)_2{\cdot}6H_2O$; 98%; Fluka) and 10 mmol of Mn^{2+} ($Mn(NO_3)_2{\cdot}4H_2O$; 98%; Fluka) was first prepared. Then, 1 M NaOH was added dropwise with stirring of the solution until pH 11 was reached. The obtained mixture was subsequently transferred into a Teflon-lined stainless steel autoclave and heated at 180 °C for 8 h. At the end, after washing several times with DW, the precipitate obtained was dried at 80 °C for 8 h. For the synthesis of $MgFe_2O_4$, using a 50 mL solution containing 5 mmol of Mg^{2+} ($Mn(NO_3)_2{\cdot}6H_2O$; 98%; Fluka) and 6.6 mmol of Fe^{3+} ($Fe(NO_3)_3{\cdot}9H_2O$; 98%; Fluka), the same procedure was repeated.

The above hydrothermal route was also employed in the synthesis of $x$$CoMn_2O_4$–$y$$MgFe_2O_4$ nanocomposites with different molar (x/y) ratios. For example, to synthesize the nanocomposite material with a 1 : 1 molar ratio (x/y = 1), 1.2 g $CoMn_2O_4$ (synthesized in the previous section) was ultrasonically dispersed in 50 mL DW for 15 min. Next, 5 mmol Mg^{2+} and 10 mmol Fe^{3+} were added to the mixture, and the pH of the medium was adjusted to 11 by adding NaOH solution (1 M) drop by drop while stirring the mixture. The mixture was then transferred into the autoclave and heated at 180 °C for 8 h. At the end, the obtained composite precipitate was washed several times with DW and dried at 80 °C for 8 h. To synthesize the other composites with the molar ratios of x/y = 2/1, 1/2 and 1/3, the same procedure was employed and the initial amounts of $CoMn_2O_4$ were 2.4, 0.6, and 0.4 g, respectively.

For the preparation of the ternary rGO/$CoMn_2O_4$–$MgFe_2O_4$ nanocomposite (termed as rGO/Compos), the synthesis process was conducted in the presence of 2 wt% rGO[47] for the heterojunction composite with the molar ratio of 0.5, which exhibited the maximum performance (Fig. S1, ESI†). Therefore, for the synthesis of the rGO/Compos, a 50 mL aqueous solution containing rGO was first prepared and ultrasonically dispersed for half an hour. Then, by adding 0.6 g $CoMn_2O_4$, 5 mmol Mg^{2+} and 10 mmol Fe^{3+} to the mixture, the composite photocatalyst was synthesized through the same hydrothermal method described above. The photocatalyst preparation steps are depicted in Fig. 1.

2.2 Material characterization

For characterization of the synthesized materials, we employed various techniques including X-ray diffraction (XRD), X-ray photoelectron spectroscopy (XPS), Fourier transform infrared (FTIR), photoluminescence (PL) and diffuse reflectance (DR) UV-Visible spectroscopies, vibrating sample magnetometry (VSM), field emission scanning electron and high-resolution transmission electron microscopies (FESEM and HRTEM), and the Mott–Schottky method. XRD patterns, XPS, and VSM data were obtained using a Philips X'Pert Pro X-ray diffractometer (λ = 1.54 D; Cu Kα beam), a SPECS Phoibos 100 (1D-DLD) analyzer (excitation: 1486.61 eV) and a vibrating sample magnetometer (Magnetic Daghigh Daneshpajouh Co.), respectively. To record FTIR, PL, and DR UV-Vis spectra of the photocatalyst materials, BRUKER Vector 22, Varian Cary Eclipse Fluorescence (λ_{ex} = 350 nm) and 5E UV-Vis-NIR spectrophotometers were utilized, respectively. The FESEM and HRTEM images of the synthesized materials were taken using Tescan Mira3 and JEM-2100 microscopes, respectively. Mott–Schottky diagrams were recorded at 1 kHz using an Ivium-Vertex Potentio-Galvanostat in a three-electrode setup [electrolyte: 0.5 M Na_2S (pH = 11); the working, counter, and reference electrodes were photocatalyst

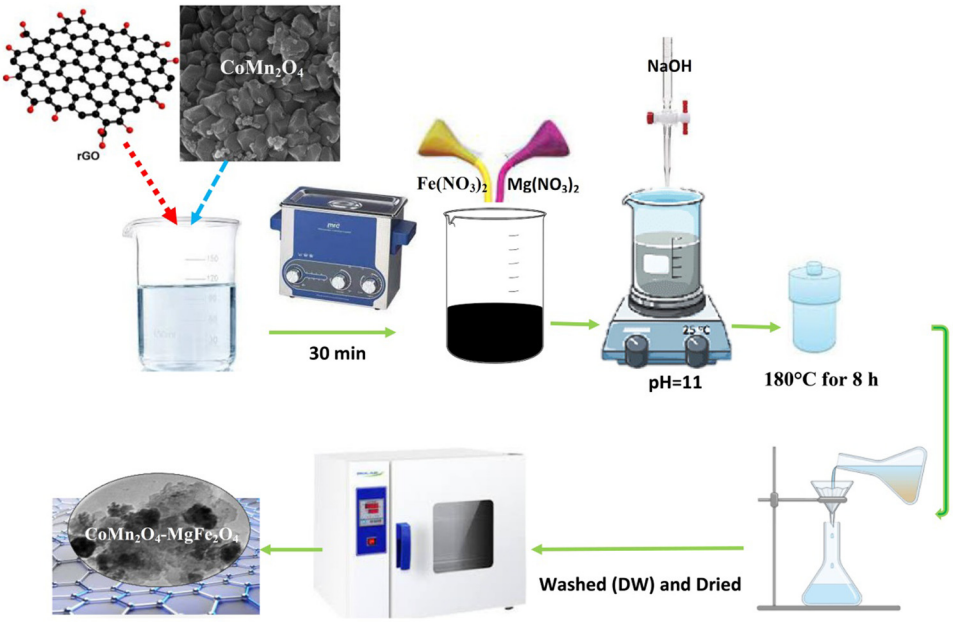

Fig. 1 Schematic representation of the photocatalyst preparation route.

film, Pt-foil (2.5 cm^2), and Ag/AgCl (3 M), respectively; for details of the approach, see ref. 6.

2.3 N_2 and bisulfide adsorption tests

Nitrogen adsorption–desorption isotherm and porosimetry data were obtained at 77 K using a BELSORB-max (BEL, Japan) instrument. In order to determine the capacity of the photocatalyst to sorb the reactant species (HS^-; see Section 2.4), a 0.5 M Na_2S solution was prepared, and its pH decreased to 11 by gradually adding a concentrated HCl to the medium [this solution is equivalent to the H_2S feed used for the conversion process, ref. 19. The bisulfide adsorption tests were conducted for the photocatalyst materials in the mentioned medium (solid to liquid ratio: 4 g L^{-1}) at 25 °C in a sealed beaker under magnetically stirring conditions. After a fixed solid–liquid contact time (3 h), the photocatalyst powder was separated through a vacuum filter using a Büchner funnel, followed by drying at 70 °C overnight. The amount of S adsorbed by the photocatalyst (mass percent) was measured using a SC-144DR sulfur and carbon analyzer. Each test was repeated at least twice and the mean value was reported as final data.

2.4 Photoreactor setup and H_2S conversion to hydrogen fuel

The photoreactor employed in this work was a handmade vertical double-walled T-controlling cylindrical glass vessel illuminated by xenon light with the intensity adjusted to 1 sun (100 mW cm^{-2}).[48,49] The capacity of the reactor was 50 mL and the reaction medium was an alkaline H_2S-saturated feed at pH = 11 ($H_2S + OH^- \rightleftharpoons HS^- + H_2O$[8,19]), containing 0.2 g photocatalyst powder–suspended magnetically during the process.[19,50] The pH of the medium was set to 11, because at this pH, bisulfide (HS^-) is the dominant species and the maximum performance (H_2 production) is achieved.[8,19] The amount of hydrogen gas released during the photoconversion process was measured every 10 min through a volumetric method described in detail elsewhere.[51]

3. Results and Discussion

3.1 Photocatalyst synthesis and characterization

The X-ray diffraction (XRD) patterns of graphite (G), graphene oxide (GO), and reduced graphene oxide (rGO) are shown in Fig. 2(a). The examination of this figure clearly indicates that the peak around 27° is the characteristic (002) peak of graphite,[52,53] whose intensity significantly decreases by exfoliation/oxidation of graphene layers and production of GO. Also, the appearance of a peak at *ca.* 13° is known as the characteristic XRD peak of GO, which is not observed in the case of G.[54,55] With the reduction of GO and synthesis of rGO, the intensity of this peak decreases, and by contrast, the intensity of the graphitic ones (peaks at 27 and 42°) is augmented. These facts and the appearance of a new peak at ~77°, all indicate the reduction of GO and successful synthesis of rGO.[54,56]

In addition to XRD, the FTIR technique was used to further corroborate the synthesis of GO and rGO; see Fig. 2(b). This figure clearly shows that during the Hummers' process and G conversion (exfoliation/oxidation) to GO, the IR bands related to O–H, C=O, C–OH and C–O functional groups emerged/are strengthened.[57,58] With the reduction of GO, the intensity of the mentioned peaks is reduced and the conversion of GO to rGO is confirmed.[57,58] N_2 adsorption–desorption studies of GO and rGO (Fig. S2, ESI†) showed a mesoporous structure (pore diameter between 2 and 50 nm) for these materials. Furthermore, by the reduction of GO, its surface area of 8.98 m^2 g^{-1} increased by about 14%.[59,60]

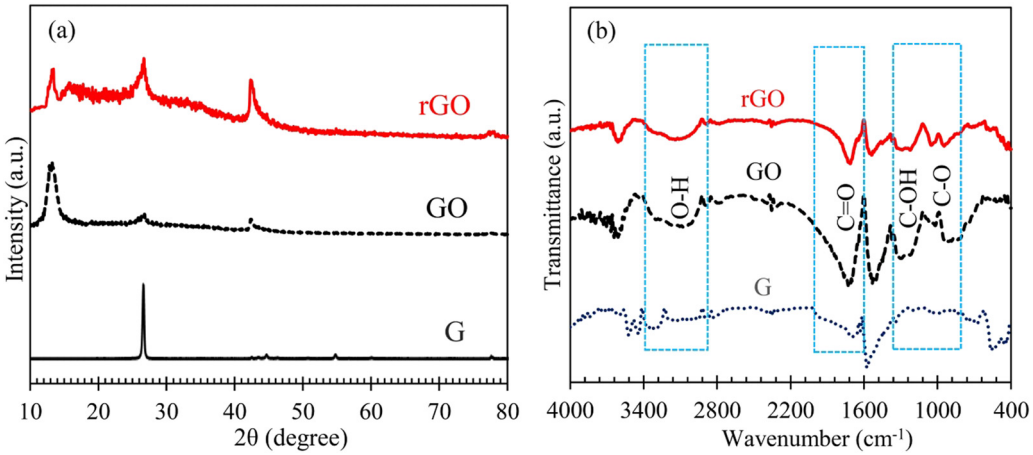

Fig. 2 XRD patterns (a) and FTIR spectra (b) of the graphite (G), graphene oxide (GO; exfoliated graphite *via* Hummers' method) and reduced graphene oxide (rGO) synthesized/employed in this work.

The XRD diagram of the composite photocatalysts is presented in Fig. 3. Examining this diagram shows that the XRD of $MgFe_2O_4$ and $CoMn_2O_4$ are consistent with JCPDS 01-073-1960 and JCPDS 00-001-1126 respectively, indicating a spinel structure for the mentioned compounds.[28,61,62] The presence of these peaks in the composite photocatalyst proved their synthesis.

In the XRD pattern of the rGO/Compos, in addition to the peaks of the Compos, the presence of the characteristic peak of rGO confirmed the successful synthesis of this composite photocatalyst/solar-energy material. Furthermore, the careful examination of the XRD diagram of rGO/Compos indicates that during the hydrothermal synthesis, the remaining GO characteristic peak (~13°; see Fig. 1(a) and 2) completely disappears. Such a phenomenon has also been seen in other works, which indicates the completion of the GO reduction–occurring during the hydrothermal process.[35,63] Regarding this fact of why the reduction of GO becomes completed during the synthesis of rGO/Compos, it can be briefly noted that under hydrothermal conditions, the superheated water (SW) in the autoclave reactor (T = 180 °C) serves as a supercritical reducing medium. Hence, further de-oxygenation of GO occurs *via* the H^+/OH^- catalyzed dehydration process,[64–67] in which SW acts as an improved electrolyte (H^+/OH^-) [notice: since water autoionization, *i.e.* $H_2O \rightleftharpoons H^+ + OH^-$ is an endothermic process, K_W increases with temperature and more protons/hydroxides are generated under supercritical/hydrothermal conditions]. In addition to XRD, the presence of components and their constituent elements in the photocatalyst materials was confirmed by EDX data (Table 1 and Fig. S3, ESI†). XPS investigations of the composite photocatalyst verified the oxidation states of +2 for Co and Mg, and +3 for Fe and Mn elements [Table 2 and Fig. S4, ESI†].

In the XPS spectra of carbon (Fig. 4), the deconvoluted peaks around 284.5, 286.4, and 287.8 eV are linked to C=C (dotted line refers to the resonance between single and double bonds), C–O, and C=O bonds of rGO, respectively.[72] With the synthesis of rGO/Compos, the intensity of the C=O peak (~287.8 eV) decreases significantly and gets almost halved [see Fig. 4(a) and (b) and compare the intensities]. This observation can be attributed to the completion of rGO reduction occurring during the hydrothermal synthesis of the rGO/Compos, which has already been recognized by the disappearance of the XRD peak at 2θ = 13° (Fig. 3).

The magnetic behavior of the heterojunction nanocomposite photocatalyst synthesized in the absence and presence of rGO is depicted in Fig. 5. Examining this figure indicates that both photocatalysts are soft ferromagnets with a saturation/spontaneous magnetization of 3.2 and 10 emu g^{-1} for Compos

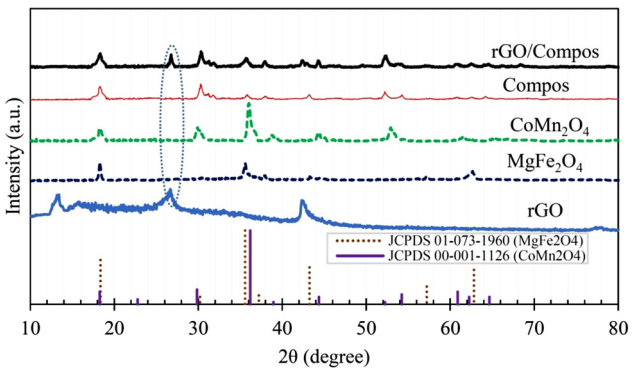

Fig. 3 X-ray diffraction (XRD) patterns of the magnetic nanocomposite solar-energy materials (Compos: $CoMn_2O_4$–$MgFe_2O_4$, rGO/Compos: rGO/$CoMn_2O_4$–$MgFe_2O_4$) along with their constituents (*i.e.* $CoMn_2O_4$, $MgFe_2O_4$, and rGO: reduced graphene oxide).

Table 1 Energy dispersive X-ray spectroscopic (EDX/EDS) data (wt%) of the photocatalyst materials synthesized in this study

Photocatalyst	Co	Mn	Mg	Fe	O	C
$CoMn_2O_4$	20.57	41.37	—	—	38.06	—
$MgFe_2O_4$	—	—	12.02	50.16	37.82	—
Compos	8.70	17.03	7.18	29.86	37.23	—
rGO/Compos	8.14	15.62	6.50	29.09	38.83	1.82

Table 2 XPS results for the composite photocatalyst in the presence of rGO

Atom	Spectral line	Binding energy[a] (eV)	Oxidation state	Ref.
Co	$2p_{3/2}$	780.6	+2	68,69
	$2p_{1/2}$	796.4		
Mn	$2p_{3/2}$	641.6	+3	28
	$2p_{1/2}$	653.3		
Mg	$2p_{3/2}$	49.5	+2	31
	$2p_{1/2}$	61.3		
Fe	$2p_{3/2}$	712.5	+3	70,71
	$2p_{1/2}$	725.2		
C	1s	284.5, 286.4, 287.8	+2, +1, 0	72,73
O	1s	529.4, 530.8, 531.6	−2	42,74–76

[a] Binding energies were corrected with respect to 284.8 eV (the adventitious C 1S peak).[6]

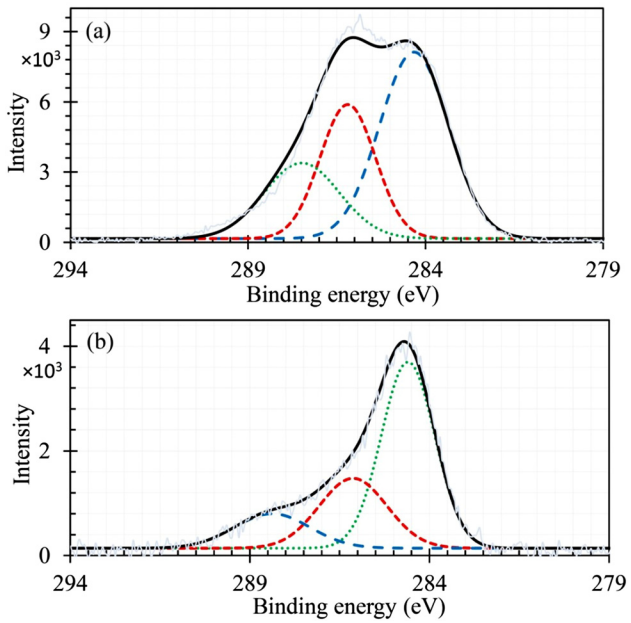

Fig. 4 XPS spectra of C (1s) recorded for (a) pristine rGO and (b) rGO/Compos [the noisy and corresponding smooth curves represent raw and enveloped data; for the survey spectra, see Fig. S4a and S5, ESI†].

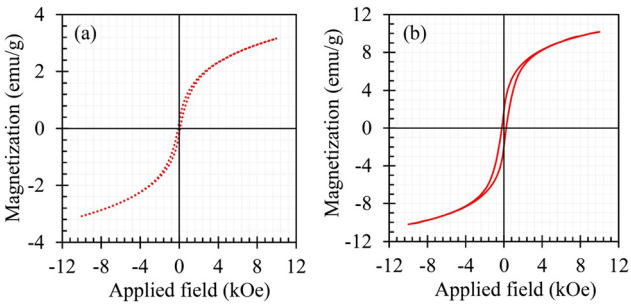

Fig. 5 Magnetic hysteresis loop of the heterojunction composite photocatalyst (Compos) in the absence (a) and presence of rGO (b).

and rGO/Compos materials, respectively.[77,78] It should be noted that the magnetic property of the Compos material is due to the $MgFe_2O_4$ component [magnetization: ~22 emu g^{-1}; see Fig. S6, ESI†]. Furthermore, the incorporation of rGO into the composite photocatalyst significantly enhances its magnetic properties. To the best of our knowledge, although no specific reason was reported for the mentioned effect, it is generally believed that rGO could facilitate electron hopping/transfer[79,80] in the composite network, improving the magnetic property of the rGO/Compos in comparison to that of Compos alone.

Scanning electron micrographs of the composite photocatalyst in the absence and presence of rGO are shown in Fig. 6. It is evident that in the presence of rGO (Fig. 6(c)), the morphology of the photocatalyst (Fig. 6(a)) is changed and a hybrid/combined structure (Fig. 6(b)) appears for the resulting rGO/photocatalyst composite [for additional images and BET data of the components, refer to the ESI,† Fig. S7, S8, and S2].

The layered morphology of rGO and the placement/deposition of the composite (Compos) nanoparticles on it were further confirmed through HRTEM observations; see Fig. 7 [for the images of $CoMn_2O_4$ and $MgFe_2O_4$, refer to Fig. S9, ESI†].

The porous morphology recognized through microscopic images for the composite photocatalyst was also verified *via* N_2 adsorption/desorption analyses conducted in the absence and presence of rGO (Fig. 8). A pore diameter of 39.8 nm was obtained for Compos, which was reduced to 10.1 nm by compositing the Compos photocatalyst with rGO. Furthermore, the presence of rGO caused a three-fold increase in the surface area of the resulting composite photocatalyst (Fig. 8, compare the *s* values).

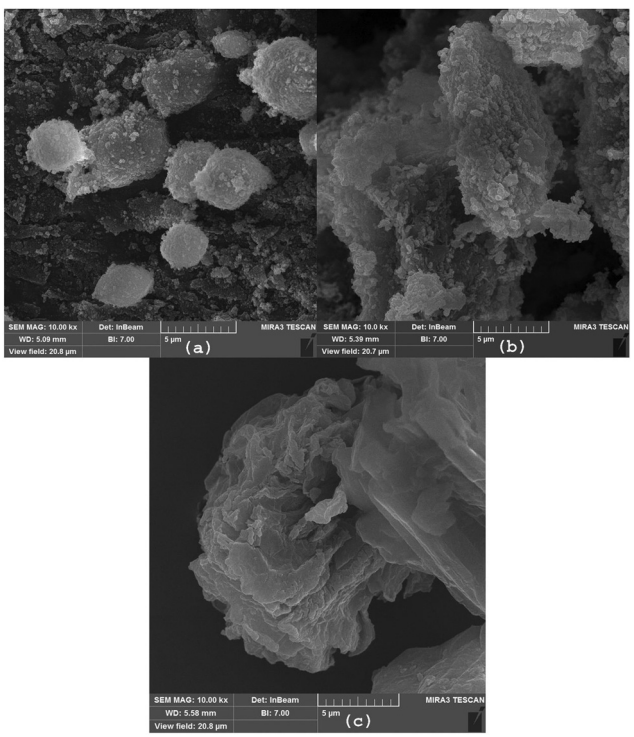

Fig. 6 FESEM images of the magnetic nanocomposite photocatalyst taken in the absence (a) and presence (b) of rGO (c).

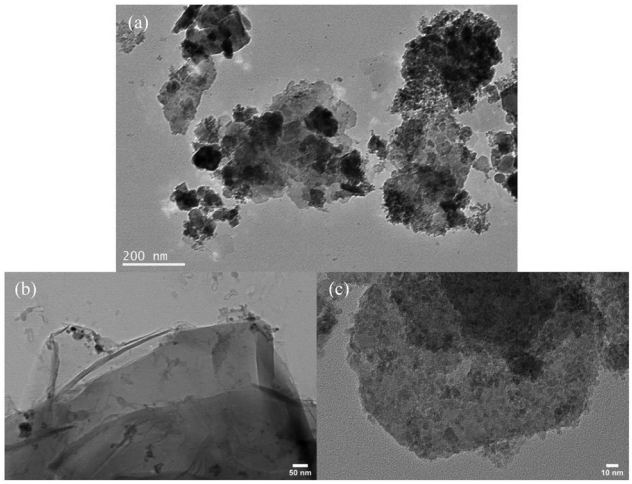

Fig. 7 HRTEM images of the nanocomposite photocatalyst (Compos; a), rGO (b), and rGO/Compos (c).

3.2 Determining factors on photocatalyst activity for effective hydrogen fuel production using H_2S feed

In addition to having a high surface area, an efficient photocatalyst material should be able to harness photons in the visible region and exhibit low recombination between photogenerated e/h pairs.[2,6] Fig. 9 shows that the composite photocatalyst synthesized in this work can absorb photons in a wide UV-Vis region and by compositing with rGO, not only the ability of the photocatalyst to absorb incident light increases (Fig. 9(a)) but the extent of charge recombination (PL emission) is also diminished (Fig. 9(b)). The good ability of the Compos to harness photons can be attributed to the presence of $MgFe_2O_4$ and $CoMn_2O_4$ semiconducting components, which serve as a superior light absorber ($SC \xrightarrow{h\nu} e_{CB}^- + h_{VB}^+$) and preventer of charge recombination ($e_{CB}^- + h_{VB}^+ \not\rightarrow$ null),[6] respectively. Concerning rGO/Compos, it should also be noted that since rGO is a good electronic (e/h) conductor,[81] the charge transfer can be facilitated within the composite material, thereby improving the charge separation and hence boosting the photocatalyst activity.[47] By utilizing the absorption data and Kubelka–Munk approach,[48] the band gap of the Compos photocatalyst was determined to be around 1.5 eV (refer to Fig. S12, ESI†). Moreover, the incorporation of rGO and the synthesis of rGO/Compos resulted in a reduced bandgap of ~1.2 eV, indicating the enhanced ability of the photocatalyst/solar-energy material to harness more photons.

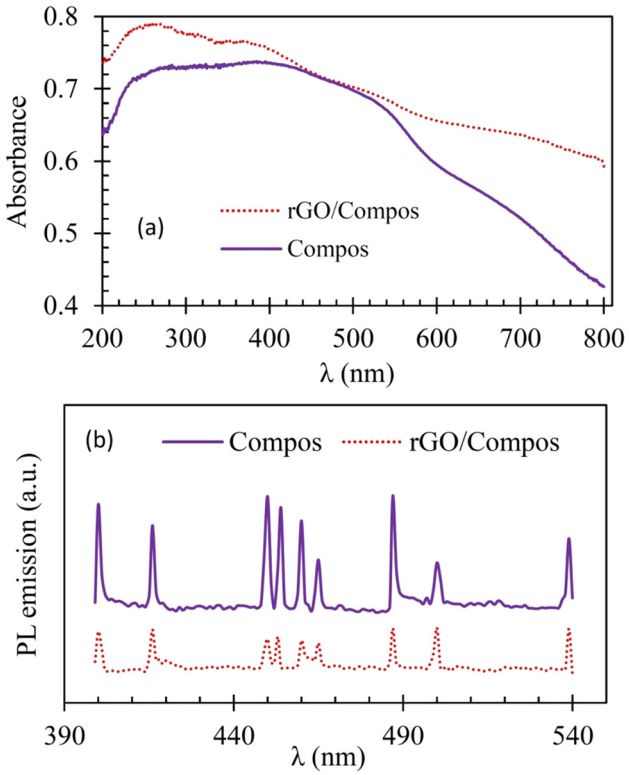

Fig. 9 Diffuse reflectance (DR) UV-visible (a) and photoluminescence (PL; b) spectra of the Compos and rGO/Compos photocatalyst/solar-energy materials under consideration [for spectra of $CoMn_2O_4$ and $MgFe_2O_4$, refer to the ESI† (Fig. S10)].

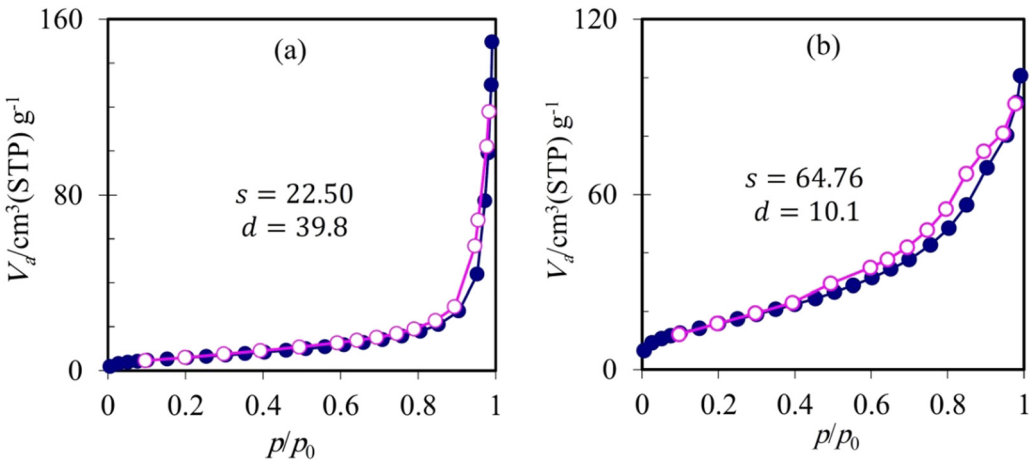

Fig. 8 Nitrogen adsorption–desorption (BET) isotherms of the composite photocatalyst (Compos) in the absence (a) and presence (b) of rGO (in these diagrams, *s* and *d* stand for surface area ($m^2\ g^{-1}$) and mean pore diameter (nm), respectively).

The photocatalytic production of hydrogen gas using H_2S feed can be well rationalized taking into account that bisulfide–the dominant species in the reaction medium–plays a crucial role during the photo-transformation process. The reactant species is initially adsorbed on the photocatalyst surface and subsequently converted to hydrogen fuel through the following reduction reaction:[8,13]

$$2HS^- + 2e_{CB}^- \rightarrow H_2\uparrow + 2S^{2-} \quad (1)$$

Therefore, it is expected that a photocatalyst with higher bisulfide adsorption capacity (BAC) and superior light absorption ability should produce more hydrogen gas. The mentioned adsorption capacity was measured for the composite photocatalysts under consideration and the results are presented in Table 3.

The data listed in Table 3 indicate that both composite photocatalysts have a good ability to adsorb bisulfide anions. By adding rGO and making rGO/Compos, the adsorption capacity is improved and the production of more hydrogen gas is anticipated. Table 3 also reveals that by adsorption of bisulfide on the photocatalyst surface, the pH of the medium increases. This fact can be rationalized in terms of the equilibrium existing between sulfide and bisulfide species in the alkaline reaction medium:[19]

$$+\begin{cases} S_{aq}^{2-} + H_2O \rightleftharpoons HS_{aq}^- + OH_{aq}^- \\ HS_{aq}^- + \text{Surface} \rightleftharpoons HS_{ads}^- \end{cases}$$
$$S_{aq}^{2-} + H_2O + \text{Surface} \rightleftharpoons HS_{ads}^- + OH_{aq}^- \quad (2)$$

Eqn (2) shows that by the adsorption of bisulfide (= its removal from the aqueous solution), the equilibrium is shifted to the right, *i.e.* the production of more hydroxide anions [Le Châtelier's principle]. Therefore, the pH increase is justified. Regarding bisulfide adsorption by the composite photocatalysts, it should also be noted that between $MgFe_2O_4$ and $CoMn_2O_4$ components, the latter is mainly responsible for the adsorption of bisulfide anions on the photocatalyst material (Table S1, ESI†). To rationalize the good capacity of $CoMn_2O_4$ in bisulfide adsorption, it should be noted that both metallic cations, particularly Co^{2+} can strongly interact with sulfide species ($K_{SP}(CoS) \leq 4.0 \times 10^{-21}$, $K_{SP}(MnS) \leq 2.5 \times 10^{-10}$;[82] $HS^- \rightleftharpoons H^+ + S^{2-}$), providing a reason why Co/Mn-containing materials could exhibit good adsorption.[83–85]

Among the photocatalyst materials synthesized in this work, owing to the high surface area, strong absorption of photons across a broad range of the UV-Vis. spectrum, low charge recombination, and good potency to adsorb the reactant species, the composite rGO/Compos photocatalyst should exhibit the highest H_2 release. Fig. 10 confirms this prediction, showing that the maximum performance (hydrogen evolution) is attained upon the mentioned photocatalyst material. Specifically, the rGO/Compos yields approximately 120 mL of H_2 gas after 3 hours of illumination, surpassing the Compos photocatalyst by around 50%.

Table 3 Ability of photocatalysts to adsorb bisulfide anions from the reaction medium [initial pH: 11; data reported as mass percentage of sulfur sorbed by the photocatalyst material]

Photocatalyst	S (wt%)	pH[a]
Compos	4.02	11.57
rGO/Compos	4.57	11.59

[a] Measured at the end of the adsorption process.

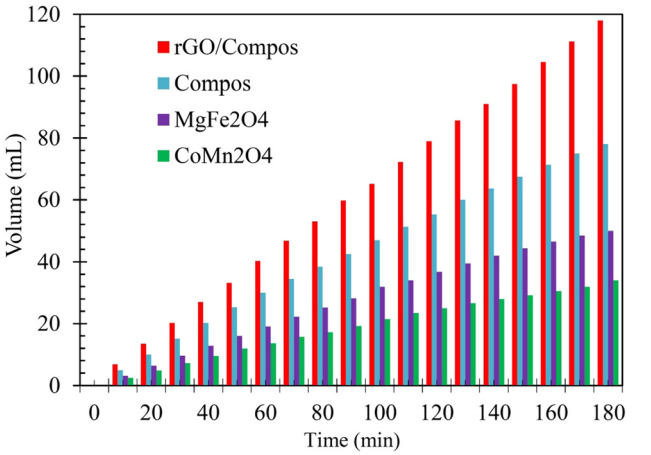

Fig. 10 Volume of hydrogen gas evolved photocatalytically as a function of irradiation time (data recorded every 10 min under atmospheric pressure at 298 K; the reaction chamber contained 0.2 g of photocatalyst powder dispersed in a 50 mL H_2S alkaline solution).

Fig. 10 also demonstrates that the lowest photocatalytic activity is due to the $CoMn_2O_4$ component. Concerning this observation, we should clarify that despite its highest BAC, $CoMn_2O_4$ cannot serve as a good photocatalyst, because of its poor photon absorption (harnessing incident light) and lowest surface area (Fig. S10 and S8, ESI†). Regarding rGO/Compos, which showed the highest gas release, it should finally be noted that this recyclable composite photocatalyst/solar-energy material has adequate photostability and the decline in its activity is insignificant in long-term use (Fig. 11).

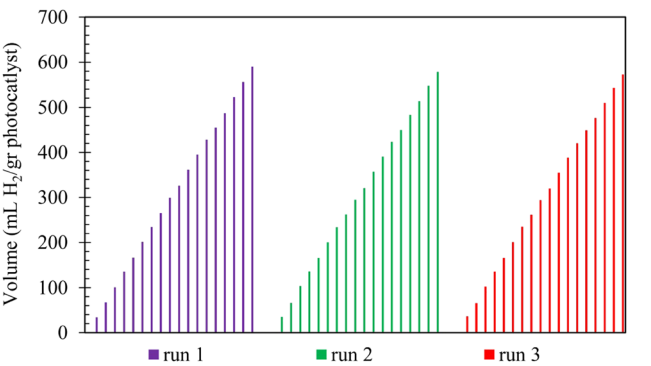

Fig. 11 Volume of hydrogen gas evolved over the rGO/Compos photocatalyst for 3 successive runs/cycles. After each run, the photocatalyst was collected and used in the subsequent test. Each run/cycle lasted 3 h and the volume of gas was recorded every 10 minutes.

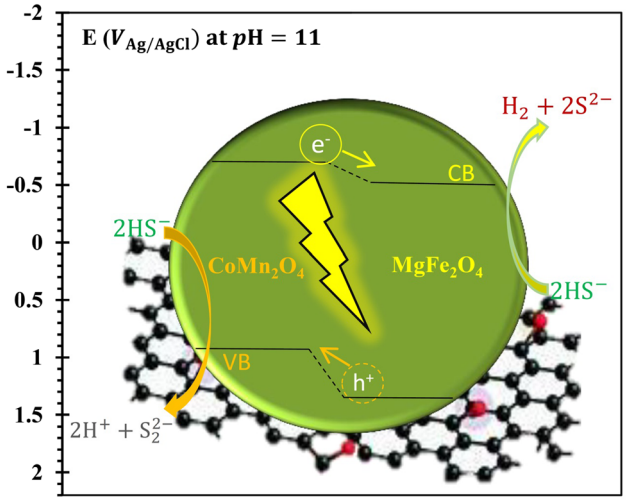

Fig. 12 Conversion mechanism and production of hydrogen gas using a bisulfide anion upon the rGO-based nanocomposite photocatalyst in the H_2S saturated alkaline medium (pH = 11) [see ref. 2, 13, 69 and 87, and Fig. S11 and S12, ESI†].

Concerning the mechanism of photocatalytic conversion of bisulfide to hydrogen fuel and the role of semiconducting components and rGO, we can briefly state that with the formation of the Compos photocatalyst ($CoMn_2O_4$–$MgFe_2O_4$), photoexcited electrons in the conduction band (CB) of the p-type component ($CoMn_2O_4$) are transferred to the CB of the n-type semiconductor ($MgFe_2O_4$), and consumed in the hydrogen production process (eqn (1)); see Fig. 12.

$$2HS^- + 2h_{VB}^+ \rightarrow S_2^{2-} + 2H^+ \quad (3)$$

Therefore, with the formation of the pn composite (Compos), the charge (e/h) separation is improved and the photogenerated charges can hence be effectively consumed in the bisulfide redox processes, resulting in a higher performance if compared to that of components alone. The presence of rGO also significantly enhanced the activity of the rGO/Compos photocatalyst (Fig. 10), in terms of improving the absorption of incident light and boosting charge transfer/separation[86] (Fig. 9), increasing the photocatalyst surface area (Fig. 8), and enhancing its adsorption capacity for the reactant species (Table 3).

4. Conclusion

In the present work, a magnetic bisulfide adsorbing nanocomposite of p-$CoMn_2O_4$/n-$MgFe_2O_4$ (Compos) and rGO (reduced graphene oxide) was synthesized using a combined Hummers'/hydrothermal method and eco-friendly affordable materials. The synthesized nanocomposite was then applied for the photocatalytic conversion of H_2S hazmat to hydrogen fuel. Based on this study, the following conclusions can be drawn:

- The photocatalytic activity of Compos is significantly boosted by adding rGO, in terms of increasing the photocatalyst surface area, enhancing its ability to absorb more photons, reducing charge recombination, and improving the adsorption of the reactant (HS^-) species.
- Bisulfide adsorption capacity investigations showed that the Compos photocatalyst has a good potency to adsorb the reactant species. Moreover, the presence of rGO further enhances the adsorption ability of the photocatalyst. The good adsorption capacity of the Compos photocatalyst is linked to the presence of the $CoMn_2O_4$ component.
- Both nanocomposite photocatalysts synthesized in this work were magnetic; by adding rGO to the Compos and synthesis of the rGO/Compos, the magnetic property of the resulting nanocomposite material was improved.
- Among different $x$$CoMn_2O_4$–$y$$MgFe_2O_4$ [r (= x/y): 0, 0.33, 0.5, 1, 2 and ∞] composites, the maximum photocatalytic activity (hydrogen production) was obtained for the composite material with r = 0.5. In the presence of rGO, the activity of Compos was promoted about 1.5 times.

Conflicts of interest

There are no conflicts of interest to declare.

Acknowledgements

The authors would like to acknowledge the anonymous Referees as well as the Editor of this journal for their useful comments to enhance the quality of the work.

References

1 A. Kumar, P. Choudhary, A. Kumar, P. H. C. Camargo and V. Krishnan, Recent advances in plasmonic photocatalysis based on TiO_2 and noble metal nanoparticles for energy conversion, environmental remediation, and organic synthesis, *Small*, 2022, **18**, 2101638.
2 M. Lashgari and M. Ghanimati, Pollutant photo-conversion strategy to produce hydrogen green fuel and valuable sulfur element using H_2S feed and nanostructured alloy photocatalysts: Ni-dopant effect, energy diagram and photoelectrochemical characterization, *Chem. Eng. Res. Des.*, 2020, **162**, 85–93.
3 A. G. De Crisci, A. Moniri and Y. Xu, Hydrogen from hydrogen sulfide: towards a more sustainable hydrogen economy, *Int. J. Hydrogen Energy*, 2019, **44**, 1299–1327.
4 M. A. Raja and V. Preethi, Performance of square and trapezoidal photoreactors for solar hydrogen recovery from various industrial sulphide wastewater using CNT/Ce^{+3} doped TiO_2, *Int. J. Hydrogen Energy*, 2019, **45**, 7616–7626.
5 Y. Uesugi, H. Nagakawa and M. Nagata, Highly efficient photocatalytic degradation of hydrogen sulfide in the gas phase using anatase/TiO_2(B) nanotube, *ACS Omega*, 2022, **7**, 11946–11955.
6 M. Lashgari and M. Ghanimati, A new efficient eco-friendly quaternary solid-solution nanoenergy material for photo-

catalytic hydrogen fuel production from H_2S aqueous feed, *Chem. Eng. J.*, 2019, **358**, 153–159.

7 M. Ferree, J. Kosco, F. Laquai, A. C. Sepulveda and D. P. S. Roman, Alerigi, Solar fuel production from hydrogen sulfide: An upstream energy perspective, *Adv. Energy Sustainability Res.*, 2023, 2200201.

8 M. Lashgari, M. Sabeti-Khabbazmoayed and M. Konsolakis, A cost-effective H_2S pollutant electro-transformation to hydrogen clean fuel and value-added semiconducting materials: A green alternative to Claus process, *J. Ind. Eng. Chem.*, 2023, **122**, 326–333.

9 H. Oladipo, A. Yusuf, S. Al Jitan and G. Palmisano, Overview and challenges of the photolytic and photocatalytic splitting of H_2S, *Catal. Today*, 2021, **380**, 125–137.

10 K. Vikrant, K. H. Kim and A. Deep, Photocatalytic mineralization of hydrogen sulfide as a dual-phase technique for hydrogen production and environmental remediation, *Appl. Catal., B*, 2019, **259**, 118025.

11 M. Balsamo, S. Cimino, G. de Falco, A. Erto and L. Lisi, ZnO–CuO supported on activated carbon for H_2S removal at room temperature, *Chem. Eng. J.*, 2016, **304**, 399–407.

12 S. B. Khan, M. S. J. Khan, K. Akhtar, E. M. Bakhsh, T. Kamal, A. M. Asiri and Y. Shen, Design of efficient solar photocatalytic system for hydrogen production and degradation of environmental pollutant, *J. Mater. Res. Technol.*, 2021, **14**, 2497–2512.

13 M. Lashgari and M. Ghanimati, An excellent heterojunction nanocomposite solar-energy material for photocatalytic transformation of hydrogen sulfide pollutant to hydrogen fuel and elemental sulfur: a mechanistic insight, *J. Colloid Interface Sci.*, 2019, **555**, 187–194.

14 H. Yi, D. Huang, L. Qin, G. Zeng, C. Lai, M. Cheng, S. Ye, B. Song, X. Ren and X. Guo, Selective prepared carbon nanomaterials for advanced photocatalytic application in environmental pollutant treatment and hydrogen production, *Appl. Catal., B*, 2018, **239**, 408–424.

15 N. Subha, M. Mahalakshmi, S. Monika, P. S. Kumar, V. Preethi, G. Vaishnavi and A. Rajabhuvaneswari, Heterostructured γ-$Fe_2O_3/FeTiO_3$ magnetic nanocomposite: An efficient visible-light-driven photocatalyst for the degradation of organic dye, *Chemosphere*, 2022, **306**, 135631.

16 D. Qiao, Z. Li, J. Duan and X. He, Adsorption and photocatalytic degradation mechanism of magnetic graphene oxide/ZnO nanocomposites for tetracycline contaminants, *Chem. Eng. J.*, 2020, **400**, 125952.

17 A. M. Ismael, A. N. El-Shazly, S. E. Gaber, M. M. Rashad, A. H. Kamel and S. S. M. Hassan, Novel $TiO_2/GO/CuFe_2O_4$ nanocomposite: A magnetic, reusable and visible-light-driven photocatalyst for efficient photocatalytic removal of chlorinated pesticides from wastewater, *RSC Adv.*, 2020, **10**, 34806–34814.

18 M. Ma, Y. Yang, Y. Chen, Y. Ma, P. Lyu, A. Cui, W. Huang, Z. Zhang, Y. Li and F. Si, Photocatalytic degradation of MB dye by the magnetically separable 3D flower-like $Fe_3O_4/SiO_2/MnO_2$/BiOBr-Bi photocatalyst, *J. Alloys Compd.*, 2021, **861**, 158256.

19 M. Lashgari and M. Ghanimati, Photocatalytic degradation of H_2S aqueous media using sulfide nanostructured solid-solution solar-energy-materials to produce hydrogen fuel, *J. Hazard. Mater.*, 2018, **345**, 10–17.

20 D. Benz, K. M. Felter, J. Köser, J. Thöming, G. Mul, F. C. Grozema, H. T. Hintzen, M. T. Kreutzer and J. R. Van Ommen, Assessing the role of Pt clusters on TiO_2 (P25) on the photocatalytic degradation of acid blue 9 and rhodamine B, *J. Phys. Chem. C*, 2020, **124**, 8269–8278.

21 J. Ge, Y. Zhang, Y. J. Heo and S. J. Park, Advanced design and synthesis of composite photocatalysts for the remediation of wastewater: A review, *Catalysts*, 2019, **9**, 122.

22 B. O. Orimolade, B. N. Zwane, B. A. Koiki, L. Tshwenya, G. M. Peleyeju, N. Mabuba, M. Zhou and O. A. Arotiba, Solar photoelectrocatalytic degradation of ciprofloxacin at a FTO/$BiVO_4/MnO_2$ anode: kinetics, intermediate products and degradation pathway studies, *J. Environ. Chem. Eng.*, 2020, **8**, 103607.

23 M. J. Abel, V. Archana, A. Pramothkumar, N. Senthilkumar, K. Jothivenkatachalam and J. Joseph, Prince, Investigation on structural, optical and photocatalytic activity of $CoMn_2O_4$ nanoparticles prepared *via* simple co-precipitation method, *Phys. B*, 2020, **601**, 412349.

24 M. Zhu, X. Dong, M. Li, L. Jia, Y. Ma, M. Zhao and H. Cui, Using photo-induced p–n junction interface effect of $CoMn_2O_4/MnO_2$ oxidase mimetic for colorimetric determination of hydroquinone in seawater, *Anal. Chim. Acta*, 2021, **1172**, 338695.

25 S. Lee, M. Govindan and D. Kim, CoFe-based layered double hydroxide for high removal capacity of hydrogen sulfide under high humid gas stream, *Chem. Eng. J.*, 2021, **416**, 127918.

26 M. Maroño, I. Ortiz, J. M. Sánchez, L. Alcaraz, F. J. Alguacil and F. A. López, Effective removal of hydrogen sulfide using Mn-based recovered oxides from recycled batteries, *Chem. Eng. J.*, 2021, **419**, 129669.

27 H. L. Tran, M. S. Kuo, W. D. Yang and Y. C. Huang, Hydrogen sulfide adsorption by thermally treated cobalt(II)-exchanged NaX zeolite, *Adsorpt. Sci. Technol.*, 2016, **34**, 275–286.

28 J. Zheng, Y. Hu and L. Zhang, Design and construction of a bifunctional magnetically recyclable 3D $CoMn_2O_4$/CF hybrid as an adsorptive photocatalyst for the effective removal of contaminants, *Phys. Chem. Chem. Phys.*, 2017, **19**, 25044–25051.

29 M. Misra, Sh. R. Chowdhury and N. Singh, TiO_2@Au@-$CoMn_2O_4$ core-shell nanorods for photo-electrochemical and photocatalytic activity for decomposition of toxic organic compounds and photoreduction of Cr^{6+} ion, *J. Alloys Compd.*, 2020, **824**, 153861.

30 G. M. Kumar, H. D. Cho, D. J. Lee, J. Ram Kumar, C. Siva, P. Ilanchezhiyan, D. Y. Kim and T. W. Kang, Elevating the charge separation of $MgFe_2O_4$ nanostructures by Zn ions for enhanced photocatalytic and photoelectrochemical water splitting, *Chemosphere*, 2021, **283**, 131134.

31 J. Chen, D. Zhao, Z. Diao, M. Wang, L. Guo and S. Shen, Bifunctional modification of graphitic carbon nitride with

$MgFe_2O_4$ for enhanced photocatalytic hydrogen generation, *ACS Appl. Mater. Interfaces*, 2015, **7**, 18843–18848.

32 U. I. Gaya, Mechanistic principles of photocatalytic reaction in *Heterogeneous photocatalysis using inorganic semiconductor solids*, ed. U. I. Gaya, Springer Science & Business Media, Dordrecht, 2014, pp. 73–89.

33 M. Seredych and T. J. Bandosz, Reactive adsorption of hydrogen sulfide on graphite oxide/$Zr(OH)_4$ composites, *Chem. Eng. J.*, 2011, **166**, 1032–1038.

34 C. Petit, B. Mendoza and T. J. Bandosz, Hydrogen sulfide adsorption on MOFs and MOF/graphite oxide composites, *ChemPhysChem*, 2010, **11**, 3678–3684.

35 J. Jo, S. Lee, J. Gim, J. Song, S. Kim, V. Mathew, M. H. Alfaruqi, S. Kim, J. Lim and J. Kim, Facile synthesis of reduced graphene oxide by modified Hummers' method as anode material for Li-, Na- and K-ion secondary batteries, *R. Soc. Open Sci.*, 2019, **6**, 181978.

36 M. Aghajani, E. Safaei and B. Karimi, Selective and green oxidation of sulfides in water using a new iron(III) bis (phenol) amine complex supported on functionalized graphene oxide, *Synth. Met.*, 2017, **233**, 63–73.

37 N. Cao and Y. Zhang, Study of reduced graphene oxide preparation by Hummers' method and related characterization, *J. Nanomater.*, 2015, **2015**, 168125, DOI: **10.1155/2015/168125**.

38 S. Park, J. An, J. R. Potts, A. Velamakanni, S. Murali and R. S. Ruoff, Hydrazine-reduction of graphite and graphene oxide, *Carbon*, 2011, **49**, 3019–3023.

39 S. Hassanpoor and N. Rouhi, Electrochemical sensor for determination of trace amounts of cadmium(II) in environmental water samples based on MnO_2/RGO nanocomposite, *Int. J. Environ. Anal. Chem.*, 2021, **101**, 513–532.

40 S. N. Tripathi, P. Saini, D. Gupta and V. Choudhary, Electrical and mechanical properties of PMMA/reduced graphene oxide nanocomposites prepared *via* in situ polymerization, *J. Mater. Sci.*, 2013, **48**, 6223–6232.

41 H. Chen, L. Ding, K. Zhang, Z. Chen, Y. Lei, Z. Zhou and R. Hou, Preparation of chemically reduced graphene using hydrazine hydrate as the reduction agent and its NO_2 sensitivity at room temperature, *Int. J. Electrochem. Sci.*, 2020, **15**, 10231–10242.

42 Z. Yan, J. Gao, Y. Li, M. Zhang and M. Guo, Hydrothermal synthesis and structure evolution of metal-doped magnesium ferrite from saprolite laterite, *RSC Adv.*, 2015, **5**, 92778–92787.

43 D. Ghanbari and M. Salavati-Niasari, Hydrothermal synthesis of different morphologies of $MgFe_2O_4$ and magnetic cellulose acetate nanocomposite, *Korean J. Chem. Eng.*, 2015, **32**, 903–910.

44 S. Ilhan, S. G. Izotova and A. A. Komlev, Synthesis and characterization of $MgFe_2O_4$ nanoparticles prepared by hydrothermal decomposition of co-precipitated magnesium and iron hydroxides, *Ceram. Int.*, 2014, **41**, 577–585.

45 N. Garg, M. Mishra and A. K. Ganguli, Electrochemical and magnetic properties of nanostructured $CoMn_2O_4$ and Co_2MnO_4, *RSC Adv.*, 2015, **5**, 84988–84998.

46 A. Chatterjee and S. Wing, Metal–organic framework-derived MnO/$CoMn_2O_4$@N-C nanorods with nanoparticle interstitial decoration in core shell structure as improved bifunctional electrocatalytic cathodes for Li–O_2 batteries, *Electrochim. Acta*, 2020, **338**, 135809.

47 P. Zhang, H. Liu and X. Li, Plasmon-driven engineering in bimetallic CuCo combined with reduced graphene oxide for photocatalytic overall water splitting, *Appl. Surf. Sci.*, 2021, **559**, 149865.

48 M. Lashgari and M. Ghanimati, A highly efficient nanostructured quinary photocatalyst for hydrogen production, *Int. J. Energy Res.*, 2015, **39**, 516–524.

49 M. Lashgari and P. Zeinalkhani, Ammonia photosynthesis under ambient conditions using an efficient nanostructured FeS_2/CNT solar-energy-material with water feedstock and nitrogen gas, *Nano Energy*, 2018, **48**, 361–368.

50 H. Oladipo, C. Garlisi, J. Sa, E. Lewin, K. Al-Ali and G. Palmisano, Unveiling the role of bisulfide in the photocatalytic splitting of H_2S in aqueous solutions, *Appl. Catal., B*, 2020, **270**, 118886.

51 M. Lashgari and M. Ghanimati, Efficient mesoporous/nanostructured Ag-doped alloy semiconductor for solar hydrogen generation, *J. Photonics Energy*, 2014, **4**, 044099.

52 X. Jiao, Y. Qiu, L. Zhang and X. Zhang, Comparison of the characteristic properties of reduced graphene oxides synthesized from natural graphites with different graphitization degrees, *RSC Adv.*, 2017, **7**, 52337–52344.

53 P. R. Riley, P. Joshi, H. Penchev, J. Narayan and R. J. Narayan, One-step formation of reduced graphene oxide from insulating polymers induced by laser writing method, *Crystals*, 2021, **11**, 1308.

54 D. R. Rout and H. M. Jena, Removal of malachite green dye from aqueous solution using reduced graphene oxide as an adsorbent, *Mater. Today Proc.*, 2021, **47**, 1173–1182.

55 S. Gurunathan, J. W. Han, A. A. Dayem, V. Eppakayala and J. H. Kim, Oxidative stress-mediated antibacterial activity of graphene oxide and reduced graphene oxide in Pseudomonas aeruginosa, *Int. J. Nanomed.*, 2012, **7**, 5901–5914.

56 C. R. Minitha and R. T. Rajendrakumar, Synthesis and characterization of reduced graphene oxide, *Adv. Mater. Res.*, 2013, **678**, 56–60, DOI: **10.4028/www.scientific.net/AMR.678.56**.

57 J. R. do Nascimento, M. R. D'Oliveira, A. G. Veiga, C. A. Chagas and M. Schmal, Synthesis of reduced graphene oxide as a support for nano copper and palladium/copper catalysts for selective NO reduction by CO, *ACS Omega*, 2020, **5**, 25568–25581.

58 A. Kumar, A. M. Sadanandhan and S. L. Jain, Silver doped reduced graphene oxide as a promising plasmonic photocatalyst for oxidative coupling of benzylamines under visible light irradiation, *New J. Chem.*, 2019, **43**, 9116–9122.

59 S. Nasir, M. Z. Hussein, N. A. Yusof and Z. Zainal, Oil palm waste-based precursors as a renewable and economical carbon sources for the preparation of reduced graphene oxide from graphene oxide, *Nanomaterials*, 2017, **7**, 182.

60 N. N. Rabin, S. Ida, M. R. Karim, M. S. Islam, R. Ohtani, M. Nakamura, M. Koinuma, L. F. Lindoy and S. Hayami, Super dielectric materials of two-dimensional TiO_2 or $Ca_2Nb_3O_{10}$ nanosheet hybrids with reduced graphene oxide, *ACS Omega*, 2018, **3**, 2074–2083.

61 X. Yuan, H. Wang, Y. Wu, X. Chen, G. Zeng, L. Leng and C. Zhang, A novel SnS_2–$MgFe_2O_4$/reduced graphene oxide flower-like photocatalyst: solvothermal synthesis, characterization and improved visible-light photocatalytic activity, *Catal. Commun.*, 2015, **61**, 62–66.

62 S. El Shabrawy, C. Bocker and C. Russel, Crystallization of $MgFe_2O_4$ from a glass in the system $K_2O/B_2O_3/MgO/P_2O_5/Fe_2O_3$, *Solid State Sci.*, 2016, **60**, 85–91.

63 Y. Wang, G. Hua, Y. Cao, Z. Peng and K. Du, One-pot synthesis of pre-reduced graphene oxide for efficient production of high-quality reduced graphene oxide and its lithium storage application, *Mater. Chem. Phys.*, 2021, **265**, 124523.

64 Y. Zhou, Q. Bao, L. A. L. Tang, Y. Zhong and K. P. Loh, Hydrothermal dehydration for the green reduction of exfoliated graphene oxide to graphene and demonstration of tunable optical limiting properties, *Chem. Mater.*, 2009, **21**, 2950–2956.

65 J. Feng, Y. Ye, M. Xiao, G. Wu and Y. Ke, Synthetic routes of the reduced graphene oxide, *Chem. Pap.*, 2020, **74**, 3767–3783.

66 N. Díez, A. Śliwak, S. Gryglewicz, B. Grzyb and G. Gryglewicz, Enhanced reduction of graphene oxide by high-pressure hydrothermal treatment, *RSC Adv.*, 2015, **5**, 81831–81837.

67 N. Akiya and P. E. Savage, Roles of water for chemical reactions in high-temperature water, *Chem. Rev.*, 2002, **102**, 2725–2750.

68 T. Kavinkumar, S. Seenivasan, A. T. Sivagurunathan, Y. Kwon and D. H. Kim, Three-dimensional hierarchical core/shell electrodes using highly conformal TiO_2 and Co_3O_4 thin films for high-performance supercapattery devices, *ACS Appl. Mater. Interfaces*, 2021, **13**, 29058–29069.

69 M. Lashgari, S. Afshari, M. Ghanimati and J. Seo, SO_2 pollutant conversion to sulfuric acid inside a stand-alone photoelectrochemical reactor: a novel, green, and safe strategy for H_2SO_4 photosynthesis, *J. Ind. Eng. Chem.*, 2023, **121**, 529–535.

70 P. Xu, J. Zheng, F. Jing and W. Chu, Influence of support precursor on FeCe–TiO_2 for selective catalytic reduction of NO with ammonia, *Mol. Catal.*, 2021, **508**, 111586.

71 L. Li, P. Ma, S. Hussain, L. Jia, D. Lin, X. Yin, Y. Lin, Z. Cheng and L. Wang, FeS_2/carbon hybrids on carbon cloth: a highly efficient and stable counter electrode for dye-sensitized solar cells, *Sustainable Energy Fuels*, 2019, **3**, 1749–1756.

72 M. Adel, M. A. Ahmed and A. A. Mohamed, Synthesis and characterization of magnetically separable and recyclable crumbled $MgFe_2O_4$/reduced graphene oxide nanoparticles for removal of methylene blue dye from aqueous solutions, *J. Phys. Chem. Solids*, 2021, **149**, 109760.

73 M. Lashgari, Fundamental aspects of CO_2 transformation into C/H/O based fuels/chemicals, *Nanomaterials for CO_2 Capture, Storage, Conversion and Utilization*, Elsevier, 2021, pp. 283–305, DOI: 10.1016/B978-0-12-822894-4.00015-0.

74 W. Zhao, Q. Zhong, J. Ding, Z. Deng, L. Guo and F. Song, Enhanced catalytic ozonation over reduced spinel $CoMn_2O_4$ for NO_x removal: active site and mechanism analysis, *RSC Adv.*, 2016, **6**, 115213.

75 Y. J. Heo and S. J. Park, Facile synthesis of MgO-modified carbon adsorbents with microwave-assisted methods: effect of MgO particles and porosities on CO_2 Capture, *Sci. Rep.*, 2017, **7**, 5653.

76 R. K. N. Kutty, P. R. Kasturi, J. Jaganath, S. Padmanapan, Y. S. Lee, D. Meyrick and R. K. Selvan, Structural and magnetic properties of $CoMn_2O_4$ synthesized by auto combustion method, *J. Mater. Sci.: Mater. Electron.*, 2019, **30**, 975–981.

77 A. F. Cabrera, C. R. Torres, S. G. Marchetti and S. J. Stewart, Degradation of methylene blue dye under dark and visible light conditions in presence of hybrid composites of nanostructured $MgFe_2O_4$ ferrites and oxygenated organic compounds, *J. Environ. Chem. Eng.*, 2020, **8**, 104274.

78 F. Fiorillo, G. Bertotti, C. Appino and M. Pasquale, Soft magnetic materials, ed. J. G. Webster, in *Wiley Encyclopedia of Electrical and Electronics Engineering*, John Wiley & Sons, Inc, 2016, pp.1–42.

79 Z. Wu, K. Pei, L. Xing, X. Yu, W. You and R. Che, Enhanced microwave absorption performance from magnetic coupling of magnetic nanoparticles suspended within hierarchically tubular composite, *Adv. Funct. Mater.*, 2019, **29**, 1901448.

80 J. M. Galloway, *Biotemplating arrays of nanomagnets using the biomineralisation protein Mms6*, PhD thesis, University of Leeds, 2012.

81 J. Wei, Z. Chen and Z. Tong, Engineering Z-scheme silver oxide/bismuth tungstate heterostructure incorporated reduced graphene oxide with superior visible-light photocatalytic activity, *J. Colloid Interface Sci.*, 2021, **596**, 22–33.

82 J. A. Dean, *Lange's Handbook of Chemistry*, McGraw-Hill Inc, New York, 1999, Table 8.6.

83 H. L. Tran, M. S. Kuo, W. D. Yang and Y. C. Huang, Hydrogen sulfide adsorption by thermally treated cobalt(II)-exchanged NaX zeolite, *Ads. Sci. Technol.*, 2016, **34**, 275–286.

84 L. F. Guo, K. L. Pan, H. M. Lee and M. B. Chang, High-temperature gaseous H_2S removal by Zn–Mn-based sorbent, *Ind. Eng. Chem. Res.*, 2015, **54**, 11040–11047.

85 K. Polychronopoulou, F. C. Galisteo, M. L. Granados, J. L. G. Fierro, T. Bakas and A. M. Efstathiou, Novel Fe–Mn–Zn–Ti–O mixed-metal oxides for the low-temperature removal of H_2S from gas streams in the presence of H_2, CO_2, and H_2O, *J. Catal.*, 2005, **236**, 205–220.

86 J. C. Hu, S. Sun, W. Xia, J. Wu, H. Liu and F. Wang, A biomimetic self-assembled cobaloxime@CdS/rGO hybrid for boosting photocatalytic H_2 production, *Chem. Commun.*, 2019, **55**, 14490–14493.

87 M. Lashgari, N. Shafizadeh and P. Zeinalkhani, A nanocomposite p-type semiconductor film for possible application in solar cells: photo-electrochemical studies, *Sol. Energy Mater. Sol. Cells*, 2015, **137**, 274–279.

